





## RESEARCH ARTICLE

10.1029/2021GC010218

# Characterization of Viscous Dissipative Heating in the Earth's Mantle Caused by Surface Forces

E. Devin<sup>1</sup>  and S. Zhong<sup>1</sup> 

<sup>1</sup>Department of Physics, University of Colorado at Boulder, Boulder, CO, USA

### Key Points:

- Work done at the surface of a viscoelastic solid is always balanced by energy stored elastically and energy dissipated as heat
- At short loading periods, dissipation is most often spatially concentrated in weak upper mantle layers
- At certain times, tidal forcing and climate forced mass movement may have contributed significantly to Earth's energy budget

### Correspondence to:

S. Zhong and E. Devin,  
[szhong@colorado.edu](mailto:szhong@colorado.edu);  
[emma.devin@colorado.edu](mailto:emma.devin@colorado.edu)

### Citation:

Devin, E., & Zhong, S. (2022). Characterization of viscous dissipative heating in the Earth's mantle caused by surface forces. *Geochemistry, Geophysics, Geosystems*, 23, e2021GC010218. <https://doi.org/10.1029/2021GC010218>

Received 19 OCT 2021

Accepted 14 JUL 2022

**Abstract** Viscous dissipative heating has long been discussed as a heat source in solid celestial bodies experiencing exogenic forces such as tidal forcing or surface loading. We examine the characteristics of viscous dissipative heating in a Newtonian, Maxwell viscoelastic solid in a 2D Cartesian box subjected to a surface load. The solutions are analyzed to understand the general controls on the energetics of planetary mantle that are associated with exogenic forcing. We find that work done at the surface is partitioned between dissipative and elastic terms depending on mantle viscosity, loading period, and loading wavelength. For viscosity structures with a weak upper mantle layer, dissipation is spatially concentrated in the upper mantle for short loading periods, implying that exogenic forces may play a role in the generation of weak upper mantle layers. The results are also scaled to estimate how much energy is dissipated in Earth's mantle, both present and past, during surface mass movement processes and tidal forcing. We find that the dissipation from glacial loading cycles since Mid-Pleistocene at a period of 100,000 years might contribute  $\sim 3$  mW/m<sup>2</sup> heat flux in the formerly glaciated regions, but for glacial cycles with a period of 40,000 years during the Early Pleistocene, the heat flux may have been 3 times larger at  $\sim 9$  mW/m<sup>2</sup>. We find that tidal forcing for the early Earth at 4 Ga may have contributed  $\sim 30$  TW of heat to the upper mantle, suggesting that exogenic forces have the capacity to contribute significantly to early Earth's energy budget.

**Plain Language Summary** Heat in the interior of solid planets and moons comes from three main sources: heat from formation, heat from the decay of radioactive elements, and energy dissipated as heat when mantle material is deformed by external forces. In this study, we use a simple 2-dimensional model to characterize heat generated by viscous dissipation resulting from a surface loading force. We examine how dissipative heating behaves under different loading conditions and in materials with different viscosity structures in order to understand the general controls on dissipative heating in solid celestial bodies. We also scale our results to estimate how much heat might be generated on Earth during climate processes, such as glaciation and de-glaciation, and during tidal deformation. Our results suggest that in some cases, heat from external forces may strongly influence mantle dynamics and even influence the dynamic formation of layered viscosity structures. On Earth in particular, heat generated by tidal forcing around 4 billion years ago was potentially of large enough magnitude to contribute significantly to interior heat and influence the dynamics of the mantle.

## 1. Introduction

There are two major sources of heat within the Earth: primordial heat from Earth's formation and radiogenic heating via the decay of unstable isotopes of uranium, thorium, and potassium (Turcotte & Schubert, 2002). The mean heat flux from the surface of the present-day Earth is about 87 mW/m<sup>2</sup>, or about 44 TW in total (e.g., Jaupart et al., 2007; Turcotte & Schubert, 2002). For the standard geochemical model of the Earth (i.e., the bulk silicate Earth model), radiogenic heating within the crust and mantle contributes  $\sim 7$  and  $\sim 13$  TW, respectively, to the total heat flow (e.g., Sramek et al., 2013; Workman & Hart, 2005), suggesting that mantle radiogenic heat generation rate is about  $3.3 \times 10^{-12}$  W/kg or  $1.4 \times 10^{-8}$  W/m<sup>3</sup>. The Earth cools over time, both as a result of secular cooling, as heat flows from the interior of the planet to the exterior, and as a result of the depletion of these radioactive elements within the mantle.

Viscous dissipation, due to deformation of the Earth's mantle caused by forces external to solid Earth, represents a third potential major source of heat within the Earth (Turcotte & Schubert, 2002). This has been observed on moons of both Saturn and Jupiter, where tidal forces cause large scale deformation of the moon's surface and result in enough dissipation to cause volcanism on the surface (Ross & Schubert, 1987; Segatz et al., 1988). Tidal

© 2022 The Authors.

This is an open access article under the terms of the [Creative Commons Attribution-NonCommercial License](https://creativecommons.org/licenses/by-nc/4.0/), which permits use, distribution and reproduction in any medium, provided the original work is properly cited and is not used for commercial purposes.

heating is likely unimportant for the present-day Earth (e.g., Jaupart et al., 2007). Processes associated with mass movement on the Earth's surface (i.e., exogenic processes as they are ultimately driven by solar energy) including erosion-deposition, glaciation-deglaciation, long-wavelength sea-level changes, and seasonal hydrological processes also cause deformation and hence dissipative heating in the mantle. These processes operate at vastly different temporal (from 1 to  $10^5$  years) and spatial scales (from 100 to  $10^4$  km) with different strengths of forcing (i.e., corresponding to pressure load variations of equivalent water column height from  $10^{-1}$  to  $10^3$  m). Tidal forces operate on time-scales of planetary orbital and rotational periods (i.e., from hours to days) with strengths of forcing that depend on orbital parameters (e.g., Ross & Schubert, 1986).

Dissipative heating in planetary mantles generated by exogenic forcing has been computed in the contexts of tidal heating for planetary bodies including Io, Europa and Enceladus (e.g., Beuthe, 2013; Ojakangas & Stevenson, 1989; Roberts & Nimmo, 2008; Ross & Schubert, 1986; Sotin et al., 2002; Steinke et al., 2020; Tobie et al., 2005, 2008) and glaciation/deglaciation induced heating in the Earth's mantle (e.g., Hanyk et al., 2005; Huang et al., 2018). In this type of calculation, stress, deformation, and dissipative heat are determined for a viscoelastic mantle in response to an exogenic loading force. It should be pointed out that tidal heating generated in the ocean below Enceladus' icy mantle and Io's magma ocean may be significant (Tyler, 2009, 2011; Tyler et al., 2015). Using realistic mantle viscosity and glaciation/deglaciation history of the last glacial cycle (i.e., the last 100,000 years) on Earth, the dissipative heating from the glaciation-deglaciation process has been estimated to be approximately 0.03 TW over the cycle, which is significantly smaller than the present-day heat flux of 44 TW (Hanyk et al., 2005; Huang et al., 2018).

However, these previous studies mainly estimated dissipative heating during specific processes, and did not explore systematically how loading period, loading wavelength, viscosity structure, and viscosity magnitude control the dissipative heating within a planetary mantle. Furthermore, these previous studies did not examine the energetics (i.e., energy balance and exchange) in the loading system. It is unclear how different forms of energy (e.g., elastic energy and dissipative heat) and work done by the exogenic forces are exchanged in the loading system and what controls the energy exchange.

This study aims to characterize and quantify the dissipation inside a viscoelastic solid produced by a force on its surface. We systematically explore the effects of loading period and wavelengths and viscosity to gain insight into the physical processes of dissipative heat generation, storage and release of elastic energy, and work done by surface forces. Because models for the full spherical geometry tend to be very computationally intensive, we simplify the problem to a two-dimensional Cartesian box, onto the surface of which a time- and space-dependent harmonic load is applied. We calculate the work done at the surface of the box by the applied force, the energy dissipated, and the elastic energy at each point within the box for all times during the loading cycle. We then examine the effects of changing the viscosity structure, viscosity magnitude, wavelength, and period of loading on the amount of dissipative heat produced and its spatial distribution throughout the box. Despite simplifications and limitations of our loading models (e.g., Cartesian models with simple loading functions in time and space), our studies have implications and relevance to loading systems including climate-driven mass loading or tidal loading on the present-day Earth's mantle with well-constrained viscosity and also on the early Earth or other planetary bodies with poorly constrained mantle viscosity or/and external forces. Particularly, because the Earth's mantle may cool about 70 K per billion years (e.g., G. F. Davies, 1999), mantle viscosity may have been more than two orders of magnitude lower for the early Earth because of temperature-dependent viscosity (e.g., Karato, 2008; Turcotte & Schubert, 2002). This study with a general loading formulation helps estimate loading induced dissipative heat for the early Earth.

## 2. Methods

### 2.1. Governing Equations and Boundary Conditions

The Earth's mantle is modeled as an incompressible viscoelastic solid whose behavior is governed by the laws of conservation of mass and momentum. These governing equations are written (e.g., Wu & Peltier, 1982; Zhong, 1997)

$$\frac{\partial u_i}{\partial x_i} = 0, \quad (1)$$

$$\frac{\partial \sigma_{ij}}{\partial x_j} + \rho f_{i,b} = 0, \quad (2)$$

where  $u_i$  is the displacement,  $x_i$  is the  $i$ th spatial dimension,  $\sigma_{ij}$  is the stress tensor,  $\rho$  is the material density, and  $f_{i,b}$  represents a body force, in this case gravitational acceleration  $g$ .

We use a 2-dimensional Cartesian model, onto the surface of which a time and space dependent loading function is applied. This loading function  $\sigma$  is given by

$$\sigma = \sigma_0 \cos\left(\frac{2\pi x}{\lambda}\right) \sin\left(\frac{2\pi t}{T}\right), \quad (3)$$

where  $\sigma_0$  is the amplitude of the load,  $\lambda$  is the wavenumber,  $t$  is time, and  $T$  is loading period. Note that the load can be a pressure load (e.g., due to ice or water) or tidal load which for incompressible media can be treated as a load at density interfaces including the surface (e.g., Qin et al., 2014). In our calculations, the load amplitude is always taken as corresponding to a 1-m-high rock load or  $\sigma_0 = \rho g \cdot 1 \text{ m}$ . This is justified because the loading problem we consider here is linear to the load amplitude, as in nearly all loading problems with linear viscoelasticity. The sides and bottom of the box are treated as free-slip boundaries with zero normal displacement (i.e., the sides have a reflecting boundary condition), and the top of the box is treated as a deformable free surface. A schematic of this Cartesian set up and the loading function is shown in Figure 1a.

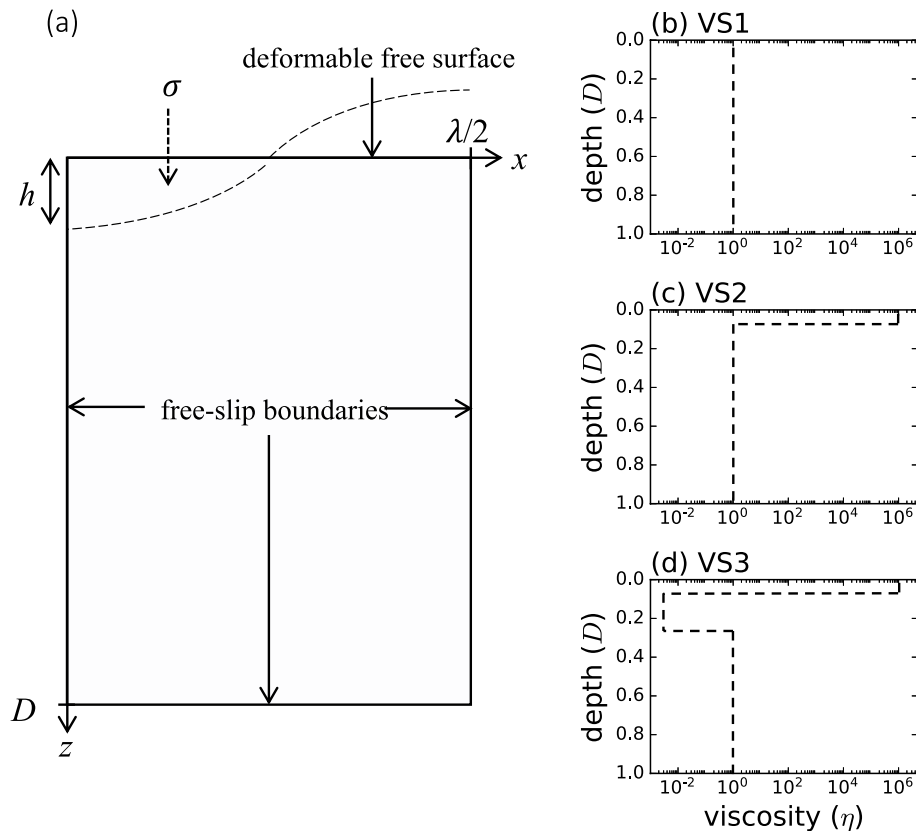


**Figure 1.** (a) A side view of the model setup. The box has a depth of  $D$  and a width of one-half the loading wavelength,  $\lambda$ . The loading function,  $\sigma$ , causes some deformation or cumulative topography of the surface, shown by the dotted line, with amplitude  $h$ . Viscosity structures designated (b) VS1, (c) VS2, and (d) VS3, with depth are plotted on the vertical axis and viscosity on the horizontal.

## 2.2. Rheology

We model the Earth's mantle using an incompressible, linear viscoelastic solid as in Zhong et al. (2003). This rheology is given by the equation

$$\sigma_{ij} + \frac{\eta}{\mu} \dot{\sigma}_{ij} = -P\delta_{ij} + 2\eta\dot{\epsilon}_{ij}, \quad (4)$$

where  $P$  represents the pressure,  $\eta$  is the viscosity,  $\mu$  is the elastic modulus,  $\delta_{ij}$  is the Kronecker delta,  $\epsilon_{ij}$  is the strain tensor, and the dot represents time derivative. Note that the Maxwell time  $\tau_M = \eta/\mu$  provides an important time-scale for stress relaxation in the media (e.g., Turcotte & Schubert, 2002). For example, if  $\eta$  and  $\mu$  are taken as  $10^{21}$  Pas and  $7 \times 10^{10}$  Pa, respectively, then  $\tau_M$  is about 455 years.

## 2.3. Energy Balance

The momentum equation (Equation 2) can be used to establish a relationship among the work done at the surface, the energy lost as heat to dissipation, and the energy stored elastically within the material via the virtual work principle. Both sides of Equation 2, assuming no internal buoyancy force, are multiplied with the incremental displacement at a given time,  $u_i$ , and integrated over the volume of the domain  $V$  by applying Green's first identity. This results in the following expression,

$$\oint_S \sigma_{ij} u_i n_j dS - \int_V \frac{\partial u_i}{\partial x_j} \sigma_{ij} dV = 0, \quad (5)$$

where  $S$  represents the boundaries for volume  $V$ , and  $n_j$  is the normal vector to the surface.

In this 2-D model, normal displacement is prohibited due to boundary conditions for all the boundaries except for the deformable top surface where the load is also applied. Therefore, the surface integral in Equation 5 is only non-zero for the top surface. On the top surface with the applied forcing or load  $\sigma$  given by Equation 3, the deformable surface has a topography,  $h$ , (i.e., cumulative displacement in vertical or normal direction at a given time  $t$ ), and the total stress  $\sigma_{22} = \rho gh + \sigma$  where subscript index two is for the vertical direction (i.e., direction of gravity). Equation 5 then becomes:

$$\oint_S \sigma u_2 dS + \oint_S \rho gh u_2 dS - \int_V \frac{\partial u_i}{\partial x_j} \sigma_{ij} dV = 0, \quad (6)$$

where the surface integrals are only for the top surface boundary. These terms can then be separated into two categories, one for the work done at the surface, and the other for the resulting strain energy within the material. The work done at the surface is given by the sum of the first two terms,

$$\Delta W = \oint_S \sigma u_2 dS + \oint_S \rho gh u_2 dS. \quad (7)$$

These two terms account for the work done by the net force at the surface. The first term represents the work done by the applied load  $\sigma$  itself, while the second term represents the work done by the surface restoring force associated with surface topography  $h$ .

The last term in Equation 6 is equal to the strain energy within the material,

$$U_{\text{strain}} = \int_V \frac{\partial u_i}{\partial x_j} \sigma_{ij} dV = \int_V \Delta \epsilon_{ij} \sigma_{ij} dV, \quad (8)$$

where  $\Delta \epsilon_{ij}$  is the strain tensor defined by incremental displacement  $u_i$  at a given time. The strain tensor can be written as follows, in terms of viscous and elastic strain,

$$\Delta \epsilon_{ij} = \Delta \epsilon_{ij}^e + \Delta \epsilon_{ij}^v. \quad (9)$$

We can rewrite the Maxwell rheological equation (Equation 4) in terms of the deviatoric stress,

$$\Delta \dot{\epsilon}_{ij} = \frac{\dot{\tau}_{ij}}{2\mu} + \frac{\tau_{ij}}{2\eta}, \quad (10)$$

or in its integral form

$$\Delta \epsilon_{ij} = \frac{\Delta \tau_{ij}}{2\mu} + \frac{1}{2\eta} \int \tau_{ij} dt, \quad (11)$$

and finally, for a small time increment  $\Delta t$ ,

$$\Delta \epsilon_{ij} = \frac{\Delta \tau_{ij}}{2\mu} + \frac{\tau_{ij} \Delta t}{2\eta}. \quad (12)$$

Equation 8 can now be rewritten in terms of deviatoric stress. In this case, since the medium is incompressible, the integral associated with the pressure vanishes. Thus, the expression becomes

$$U_{\text{strain}} = \int_V \frac{\Delta \tau_{ij} \tau_{ij}}{2\mu} dV + \int_V \frac{\tau_{ij}^2 \Delta t}{2\eta} dV = U_{\text{elastic}} + \phi, \quad (13)$$

where the first term represents energy stored elastically:

$$U_{\text{elastic}} = \int_V \frac{\Delta \tau_{ij} \tau_{ij}}{2\mu} dV, \quad (14)$$

and the second represents energy lost to heat via dissipation (e.g., Hanyk et al., 2005):

$$\phi = \int_V \frac{\tau_{ij}^2 \Delta t}{2\eta} dV. \quad (15)$$

Returning to Equation 6 and using power (i.e., energies divided by  $\Delta t$ ), we can write the statement of conservation of energy as:

$$P_{\text{work}} = P_{\text{elastic}} + P_{\phi}. \quad (16)$$

This equation states that over a time increment  $\Delta t$ , the work done at the surface (Equation 7), both that done by the load and that associated with the restoring force due to topography, is equal to the amount of energy stored elastically (Equation 14) plus the amount of energy lost to heat through dissipation (Equation 15). Since the work or power done by surface forcing  $P_{\text{work}}$  can be approximated by the total surface loads and displacement (e.g., the total ice height and the surface depression it causes), this energy balance statement (Equation 16) helps estimate the dissipation  $P_{\phi}$ , if the elastic energy is not important (e.g., when the loading period is significantly longer than Maxwell time  $\tau_M$ ).

#### 2.4. Numerical Analysis

Equations 1, 2 and 4 are solvable analytically using the Laplace transform and correspondence principle for simple models (e.g., Zhong, 1997), however we use numerical methods because we will test 345 possible configurations, many of which have inhomogeneous viscosities. The system of equations is solved numerically under the time and space dependent load given by Equation 3. This is accomplished using a finite element code called CitcomVE, which was modified from a code called Citcom, which was developed to model thermal convection in a viscous fluid (Moresi & Solomatov, 1995). CitcomVE was developed to model deformation of a viscoelastic solid for glacial isostatic adjustment and volcanic loading problems (Zhong & Watts, 2013; Zhong et al., 2003).

The governing equations are non-dimensionalized before the solutions are computed (see Zhong et al., 2003). This makes it easy to generalize the results for any viscosity, shear modulus, box depth, or loading amplitude without having to solve the equations again. Most of the results in the sections that follow will be presented in dimensionless form to keep a more general perspective, but some will be dimensionalized to compare to actual heat sources and deformation phenomena on Earth and other celestial bodies.

**Table 1**  
Viscosity Structures

Depth range ( $D$ )	Viscosity ( $\eta$ )		
	VS1	VS2	VS3
0–0.0137	1	$1 \times 10^6$	$1 \times 10^6$
0.0137–0.228	1	1	0.0333
0.228–1	1	1	1

Displacement, coordinates, and wavelength are scaled by box depth  $D$  and the dimensionless depth is defined to be 1. Viscosity and shear modulus are scaled by the lower mantle viscosity  $\eta$  and the shear modulus  $\mu$ . In this study, the shear modulus is assumed to be constant everywhere, while the mantle viscosity may differ in the upper mantle and lithosphere. Stress and pressure are scaled by the shear modulus of the material. Time is scaled by the characteristic time for stress relaxation within a viscoelastic material, the Maxwell time  $\tau_M$  of the lower mantle,  $\eta/\mu$ . Power is then scaled by a combination of these quantities in  $P_0$

$$P_0 = \frac{\mu^2 \cdot D^2 \cdot 1m}{\eta} \quad (17)$$

### 2.5. Cases of Different Parameters

We compute a total of 345 different models defined by three viscosity structures, five loading wavelengths, and 23 loading periods. The three viscosity structures are loosely based on the structure of the Earth's mantle. Viscosity structure 1 (henceforth referred to as VS1) is a uniform viscosity of  $\eta$  at all depths. Structure 2 (VS2) has a thin stiff layer ( $0.0137D$ ) of viscosity  $10^6\eta$  at the top, and viscosity of  $\eta$  for all other depths. This thin stiff layer corresponds to a 40 km thick lithosphere, taking  $D = 2,900$  km, the depth of the mantle. Structure 3 (VS3) has the same thin stiff top layer as VS2, and then a weak layer with viscosity  $0.0333\eta$  extending to a depth of  $0.23D$  (rescaled to mantle depth, this represents the upper mantle, with the interface with the lower mantle at 660 km depth), and then a viscosity of  $\eta$  in the bottom layer (i.e., the lower mantle). VS3 is motivated by viscosity models inferred from geoid studies (Hager & Richards, 1989).

These three viscosity profiles are shown in Figures 1b–1d. For each viscosity structure we test five different wavelengths  $\lambda$  ranging from  $0.625D$  to  $10D$ , and for each wavelength we test 23 different periods  $T$  from  $7.63 \times 10^{-5}\tau_M$  to  $320\tau_M$ . Tables 1–3 list the viscosity structures, wavelengths, and periods and their shorthand designations. Table 2 also lists the spatial resolution of our models. Each model is run with a timestep size optimized for solution stability, with values ranging from  $\Delta t = 0.5$ – $0.001\tau_M$  depending on the period.

## 3. Results

### 3.1. A Representative Case

We first present the results of a single case that has a uniform viscosity (i.e., VS1), a loading period of  $T = 40\tau_M$ , and a wavelength of  $\lambda = 1.25D$ , to illustrate the basic behavior of the system under the loading force. The surface of the box is incrementally displaced by the loading force. Figures 2a–2c shows the surface topography  $h$  (dashed line), incremental vertical displacement  $u_2$  (dotted line) and the loading force  $\sigma$  (solid line) plotted against the  $x$ -dimension of the box at three different times: (a)  $t = 0\tau_M$ , (b)  $t = 5\tau_M$ , and (c)  $t = 10\tau_M$ . The loading function has zero amplitude at  $t = 0\tau_M$  and reaches its maximum amplitude of  $\sigma_0 = \rho g \cdot 1m$ , where  $\rho = 3,300$  kg/m<sup>3</sup> and  $g = 10$  m/s<sup>2</sup>, at  $t = 10\tau_M$  (i.e., a quarter of the period). The topography  $h$  is the cumulative vertical displacement

of the box surface in response to the loading. At the left side of the box (i.e.,  $x = 0$ ), the loading force is positive for  $t$  from 0 to  $20\tau_M$ , and causes the surface at  $x = 0$  to subside (i.e., negative topography or  $h < 0$ ) during this time segment. At any given time, the sum of loading force and the restoring force associated with topography (i.e.,  $\sigma + \rho gh$ ) is the net vertical force acting on the surface. Note that multiplying the net vertical force with incremental vertical displacement  $u_2$  across the surface determines the work done at the surface,  $\Delta W$  as in Equation 7.

Figure 2d shows the topography  $h$  and the incremental vertical displacement  $u_2$  at the left edge of the box (i.e.,  $x = 0$ ) over time during the entire loading cycle. Note that the topography is negative in the first half of the period and

**Table 2**  
Wavelengths

Wavelength $\lambda$ ( $D$ )	Vertical nodes	Horizontal nodes	Average element size ( $D^2$ )
10.0	49	193	0.00054
5.0	49	97	0.00054
2.5	49	65	0.00041
1.25	49	33	0.00041
0.625	49	33	0.00020



**Table 3**  
Periods

	Period $T$ ( $\tau_M$ )		Period $T$ ( $\tau_M$ )
01	320	13	$7.81 \times 10^{-2}$
02	160	14	$3.91 \times 10^{-2}$
03	80	15	$1.95 \times 10^{-2}$
04	40	16	$9.76 \times 10^{-3}$
05	20	17	$4.88 \times 10^{-3}$
06	10	18	$2.44 \times 10^{-3}$
07	5	19	$1.22 \times 10^{-3}$
08	2.5	20	$6.10 \times 10^{-4}$
09	1.25	21	$3.05 \times 10^{-4}$
10	0.625	22	$1.52 \times 10^{-4}$
11	0.3125	23	$7.63 \times 10^{-5}$
12	0.156		

positive in most of the second half the period, that the maximum amplitude of the topography is less than 1 m, and that although the loading function has a period of  $40\tau_M$ , the topography has not returned to zero at the end of the loading cycle. This indicates that the material does not respond instantaneously to the applied pressure, as is to be expected with a viscous media.

As discussed in Section 2.3, the system must obey conservation of energy, and thus the rates of negative net work done at the surface, the energy stored elastically, and the energy dissipated as heat must sum to zero (i.e., Equation 16 or  $P_{\text{work}} = P_{\text{elastic}} + P_{\phi}$ ). To check that this is indeed occurring in our numerical results, we compute powers  $P_{\text{work}}$ ,  $P_{\text{elastic}}$ , and  $P_{\phi}$  associated with the work at the surface, elastic energy, and dissipation, using Equations 7, 14 and 15, respectively, all of which are divided by time increment per time step  $\Delta t$ . We define energy fluxes as powers  $P_{\text{work}}$ ,  $P_{\text{elastic}}$ , and  $P_{\phi}$  divided by the surface area of the box (i.e.,  $1 \cdot \lambda/2$ ). Note that the unit of the energy fluxes is  $\text{W/m}^2$ , the same as heat flux at the surface. The dimensionless energy fluxes associated with the negative work done by the net force at the surface, elastic energy, dissipation, and their sum for a loading amplitude of 1 m for a whole loading cycle are shown in Figure 2c. These energy fluxes are normalized by  $D\mu^2/\eta$ . The sum of elastic energy, dissipation, and negative net work lies along the zero of the y-axis, indicating that conservation of energy is indeed

satisfied for any given time. Note that at this loading period, only a small fraction of the energy added to the system as work is stored elastically, while a much larger fraction is dissipated as heat. Also, the stored elastic energy can be positive or negative (Figure 2c), suggesting that the elastic energy is both stored and released by the material at different times.

To visualize where dissipation is occurring within the box, we compute the volumetric dissipation rate (again scaled for dimensionless equivalent to a 1 m load) for each element within the box at a given time step and plot them as a contour plot. Figure 3 shows dissipation power (i.e.,  $\tau_{ij}\tau_{ij}/(2\eta)$ ) as filled contours according to the scale at left, for the box for  $t = 0.8\tau_M$  (i.e., shortly after the loading starts),  $t = 5\tau_M$ , and  $t = 10\tau_M$ . In all three timesteps, dissipation occurs mostly in the top half of the box across the width of the box and grows slightly in magnitude between each step. We expect that the spatial pattern of dissipation within the box should vary with different periods, wavelengths, and viscosity structures, and we examine these in more detail in subsequent sections.

### 3.2. Effects of Period

To understand the effects of loading period on the energy balance of this system, we again plot dimensionless dissipation, elastic energy, and negative work as energy fluxes against time throughout the loading cycle for three cases with different periods of  $320\tau_M$ ,  $20\tau_M$ , and  $0.02\tau_M$  which otherwise are identical to the representative case (i.e., VS1 and  $\lambda = 1.25D$ ) (Figure 4). As the loading period decreases, the energy flux of the work done by surface forcing increases significantly (Figure 4). This is expected because the faster the forcing, the larger the power it delivers. Note that for a long period load (Figure 4a), very little energy is stored elastically, and the dissipation is nearly equal and opposite to the negative work. That is, nearly all the work done at the surface by the loading force and the restoring force associated with topography is converted to dissipative heating. For a short period (Figure 4c), the opposite is true; very little energy is dissipated as heat, and the stored elastic energy is approximately equal and opposite to negative work.

### 3.3. Effect of Viscosity Structure and Loading Wavelength

To understand the effects of viscosity structure on dissipation, we first examine how the magnitude of dissipation produced is affected by viscosity structure at different periods. Figure 5 shows the total energy flux from dissipation (as in Figure 4) versus time for all three viscosity structures, a wavelength of  $\lambda = 1.25D$  and periods (a)  $320\tau_M$ , (b)  $20\tau_M$ , and (c)  $0.02\tau_M$ . For all periods, VS1 and VS2 are producing identical amounts of dissipation, as we would expect, given that the only difference between the two is the thin stiff layer at the top of VS2 with thickness much smaller than the wavelength. VS3 with a weak upper mantle produces significantly less dissipation

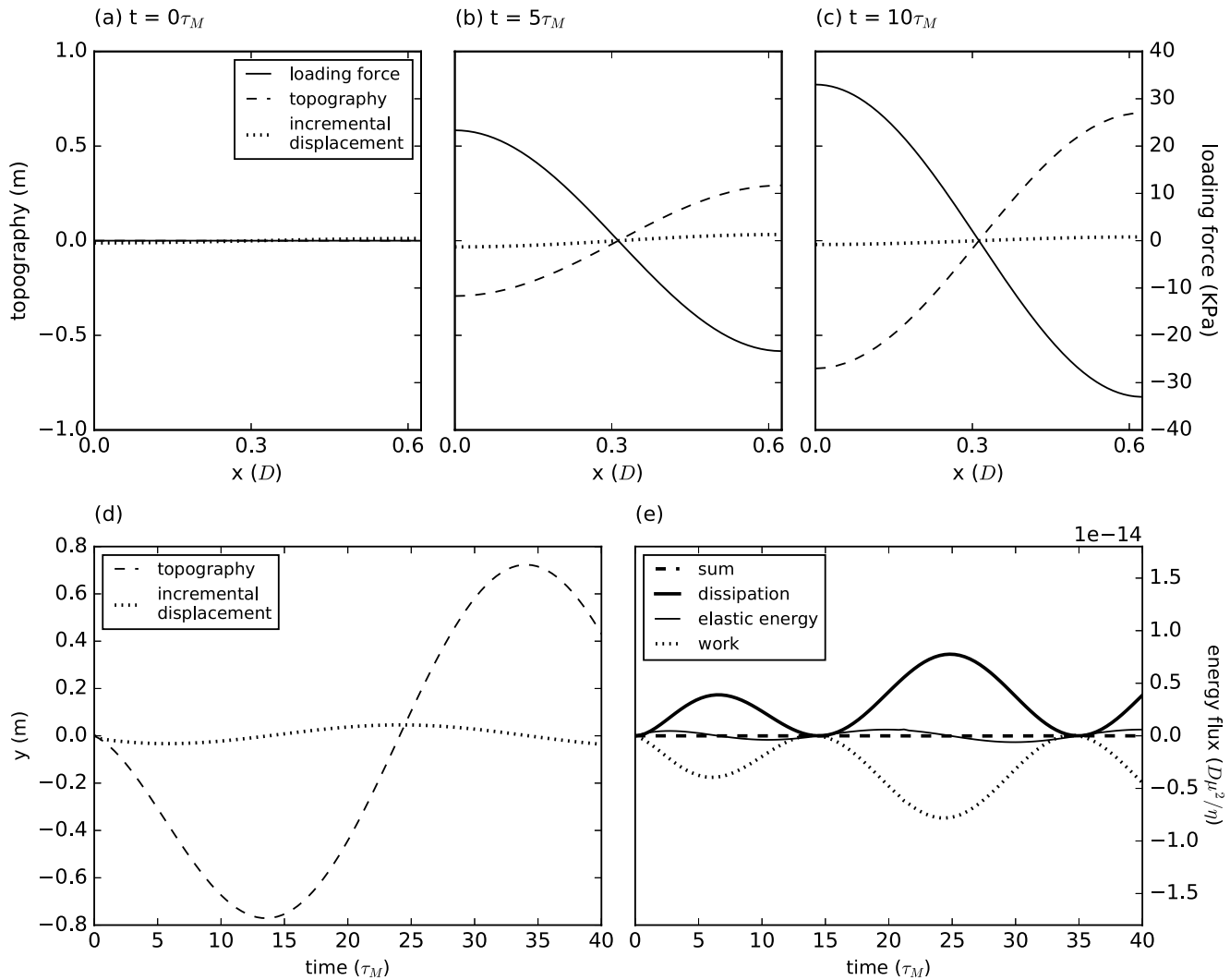


**Figure 2.** The loading force, in Pascals, the topography, in meters, and the incremental displacement, in meters, for (a)  $t = 0\tau_M$ , (b)  $t = 5\tau_M$ , and (c)  $t = 10\tau_M$  for the representative case (i.e., VS1,  $T = 40\tau_M$ , and  $\lambda = 1.25D$ ). Note that the width of the box is equal to  $\lambda/2$ . (d) The topography  $h$  and the incremental displacement  $u_2$  at the left edge of the box (i.e.,  $x = 0$ ) and (e) dimensionless energy fluxes associated with dissipation, elastic energy, negative work, and their sum as a function of time throughout the loading cycle for the representative case. The maximum amplitude of the load is  $\sigma_0 = \rho g \cdot 1 \text{ m}$  with mantle depth  $D$  of 2,900 km.

than VS1 and VS2 at long periods (Figures 5a and 5b for  $T = 320\tau_M$  and  $20\tau_M$ , respectively), but significantly more at short periods (Figure 5c for  $T = 0.02\tau_M$ ). This is also expected since VS3 has a smaller effective viscosity than VS1 and VS2, and so heat production in VS3 should be maximized at a shorter period than in VS1 and VS2.

It is also interesting to note how viscosity structure affects the spatial distribution of dissipation within the box for different periods and wavelengths. Since VS1 and VS2 have nearly identical energy fluxes (Figure 5), we focus this analysis only on VS1 and VS3 for simplicity. Figures 6 and 7 show spatial distributions of volumetric dissipation rate at an instant in time when the spatially averaged dissipation rate is at the maximum during the loading cycle plotted for three sample periods ( $T = 320\tau_M$ ,  $T = 20\tau_M$ , and  $T = 0.02\tau_M$ ) and three sample wavelengths ( $\lambda = 10D$ ,  $\lambda = 2.5D$ , and  $\lambda = 0.625D$ ) for VS1 and VS3 respectively.

As seen in Figure 6, the spatial dependence of dissipation rate for VS1 depends only on wavelength and is independent of period, although the magnitude of dissipation rate increases with decreasing period. For long wavelengths (Figures 6a, 6d and 6g for  $\lambda = 10D$ ) the dissipation extends throughout the entire depth of the box and is concentrated at the edges of the box. For short wavelengths (Figures 6c, 6f and 6i for  $\lambda = 0.625D$ ) the dissipation is concentrated in the top third of the box and extends uniformly across its width, indicating a limited reach of



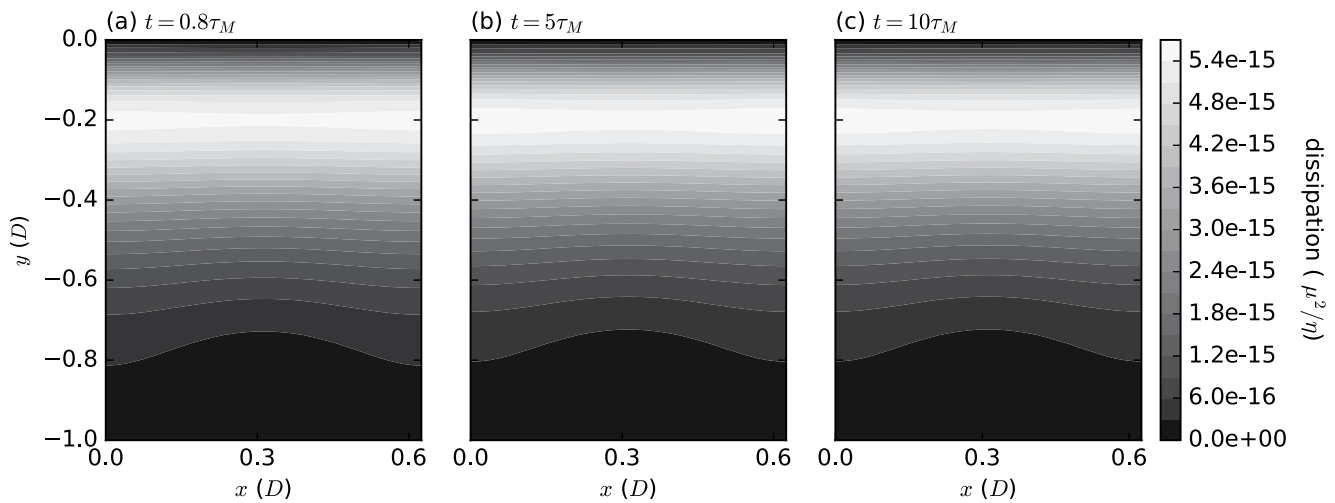
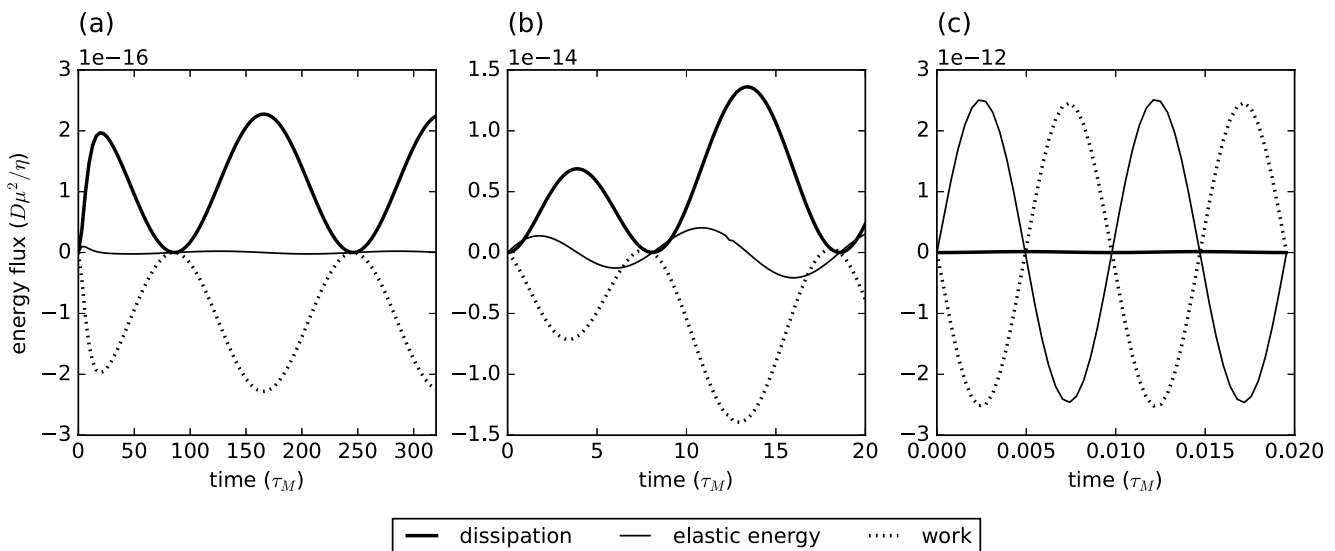


**Figure 3.** Contour plots of the dimensionless volumetric dissipation rate throughout the box for the representative case at (a)  $t = 0.8\tau_M$ , (b)  $t = 5\tau_M$ , and (c)  $t = 10\tau_M$ .

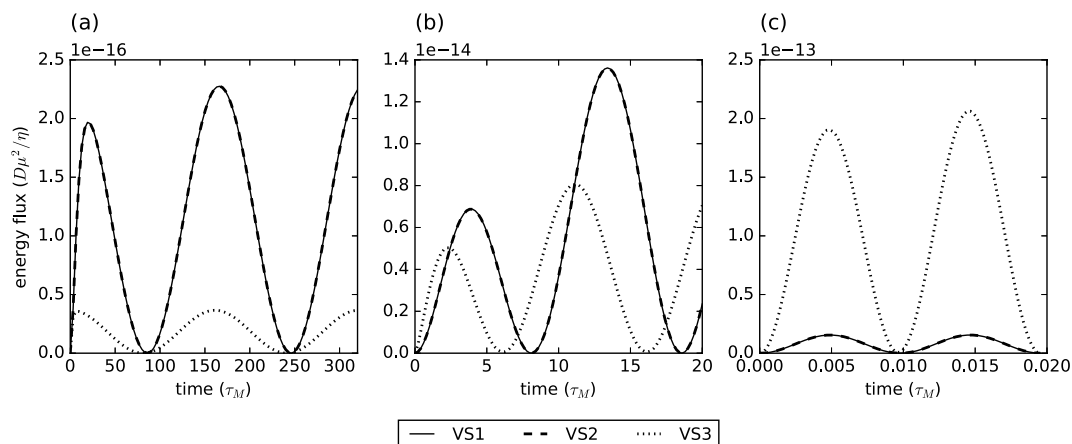
the surface loading at short wavelengths into the mantle. Although Figure 6 only shows results for three different wavelengths, the variations in the pattern are gradual with respect to wavelength.

Figure 7 shows that the spatial distribution of dissipation for VS3 is dependent on both period and wavelength. For long wavelengths and long to medium periods (Figures 7a and 7d for  $\lambda = 10D$  and  $T = 320\tau_M$  and  $20\tau_M$ ) dissipation occurs mostly in the lower mantle, concentrated at the edges of the box. However, for all other scenarios (e.g., for short period  $T = 0.02\tau_M$ , and short to intermediate wavelengths  $\lambda = 2.5D$  or less), the dissipation occurs only in the upper mantle with reduced viscosity (Figures 7b, 7c and 7e–7i). In particular, for short period and short wavelength, the dissipation is uniformly distribution in the upper mantle (Figure 7i), while for the other scenarios the dissipation is concentrated at the edges of the box or at the 670 km depth with viscosity variations. Also note that the magnitude of dissipation is significantly larger for VS3 than VS1 for short periods (Figures 7g–7i for VS3 vs. Figures 6g–6i for VS1, and also see Figure 5).

Figures 6 and 7 are not necessarily representative of the distribution of dissipation over the entire period since they show only an instant in time with maximum total dissipation. To understand how the distribution of dissipation varies with depth over an entire loading cycle, we average the dissipation produced in each row of elements



**Figure 4.** Dimensionless dissipation, elastic energy, and negative work as energy fluxes plotted against time throughout the loading cycle, scaled again for 1 m dimensionless equivalent load, for VS1 and  $\lambda = 1.25D$  with periods (a)  $320\tau_M$ , (b)  $20\tau_M$ , and (c)  $0.02\tau_M$ .



**Figure 5.** Energy flux from dissipation plotted over time all three viscosity structures, a wavelength of  $\lambda = 1.25D$  and periods of (a)  $320\tau_M$ , (b)  $20\tau_M$ , and (c)  $0.02\tau_M$ .

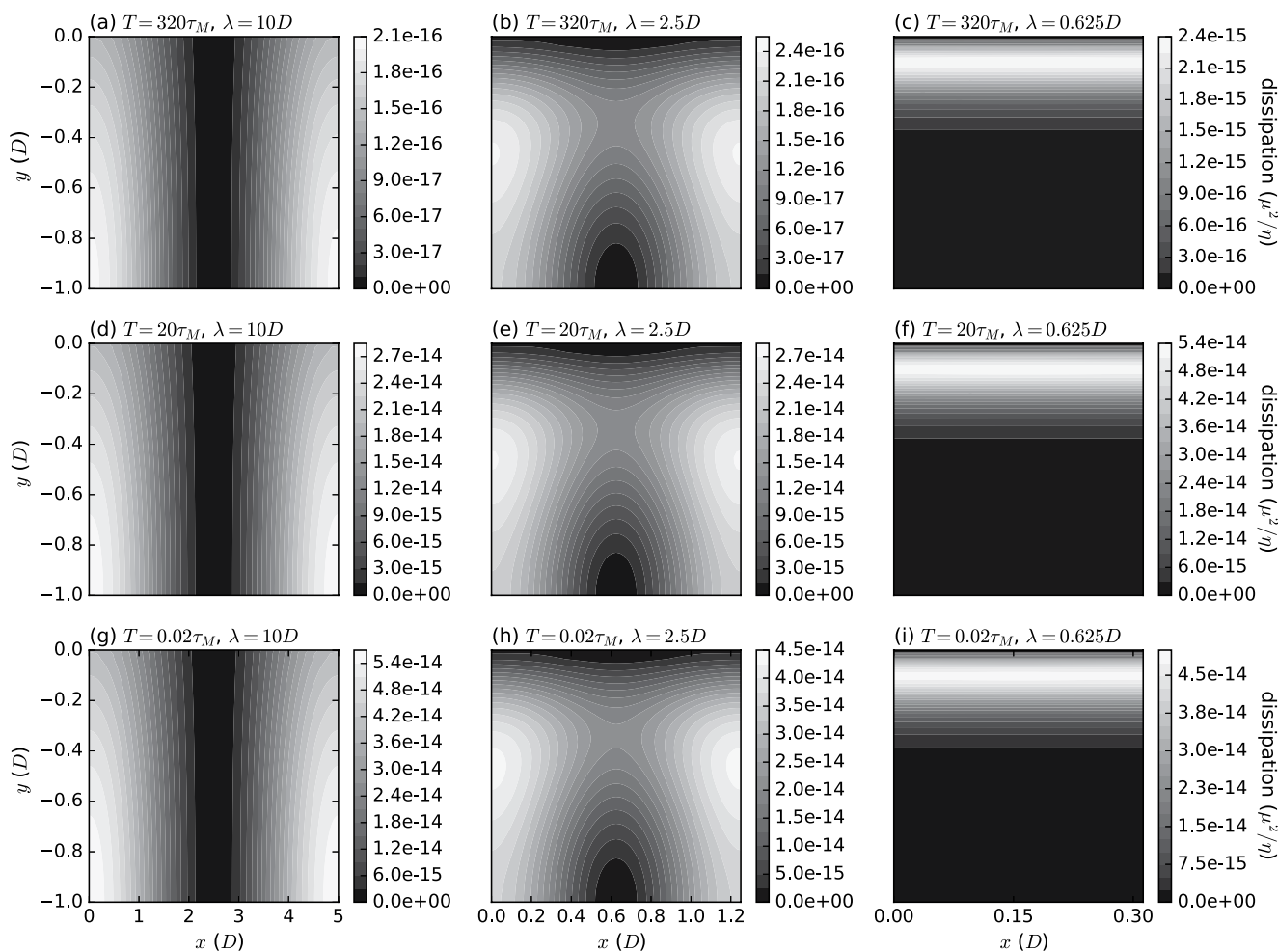


**Figure 6.** Contour plots of the volumetric dissipation rate when the dissipation rate is at maximum during the loading cycle for VS1 cases with periods (top row)  $320\tau_M$ , (middle row)  $20\tau_M$ , and (bottom row)  $0.02\tau_M$  and with wavelengths (first column)  $10D$ , (middle column)  $2.5D$ , and (last column)  $0.625D$ .

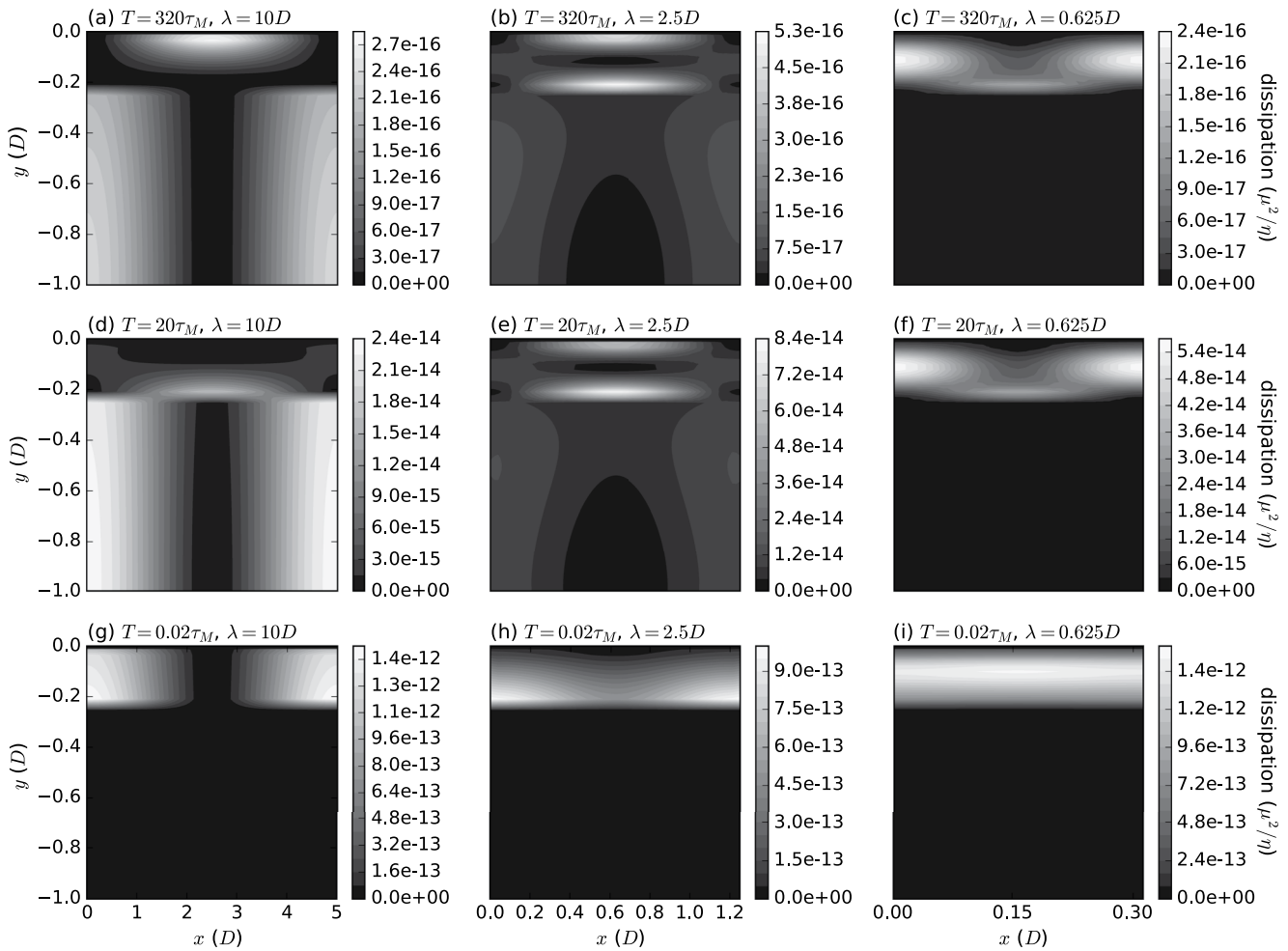


**Figure 7.** Contour plots of the volumetric dissipation rate when the dissipation rate is at maximum during the loading cycle for VS3 cases with periods (top row)  $320\tau_M$ , (middle row)  $20\tau_M$ , and (bottom row)  $0.02\tau_M$ , and with wavelengths (first column)  $10D$ , (middle column)  $2.5D$ , and (last column)  $0.625D$ .

over both time and horizontal distance and plot this value as a function of depth, as shown in Figure 8, again for VS1 and VS3 respectively. This plot shows approximately the same trends as seen in the contour plots above (Figures 6 and 7). For VS1 models (solid line in Figure 8), the depth-distribution of dissipation only depends on wavelength, and the shorter the wavelength, the shallower depth the dissipation occurs, independent of period. For VS3 (dashed line in Figure 8), the distribution of dissipation is dependent on both period and wavelength. For short wavelengths, dissipation is concentrated in the weak upper mantle for all periods (Figures 8b and 8c for  $\lambda \leq 2.5D$ ), but for long wavelengths, dissipation occurs mostly in the upper mantle for only short periods (Figure 8g). For long wavelengths and long periods, dissipation is concentrated in the lower mantle (Figures 8a and 8d). Importantly, for short periods, the dissipation is concentrated in the weak upper mantle with peak amplitudes in VS3 models that are  $\sim 30$  times larger than that in VS1 models (Figures 8g–8i and for  $T = 0.02\tau_M$ ). The finding that the dissipation is concentrated in the weak upper mantle layer is similar to that in Hanyk et al. (2005) and Steinke et al. (2020), but our study also shows that for long-wavelength loading at relatively long periods (e.g.,  $\lambda = 10D$  and  $T \geq 20\tau_M$  in Figures 7a, 7d, 8a, and 8d), more dissipation occurs in the high viscosity lower mantle.

### 3.4. Efficiency

As shown in Figures 2e and 4, a portion of the energy added to this system as work by surface force is stored elastically by the material, and a portion of it is dissipated as heat. The time-averaged power in terms of energy flux for both dissipation and work are computed for each case to examine how much of the work done at the

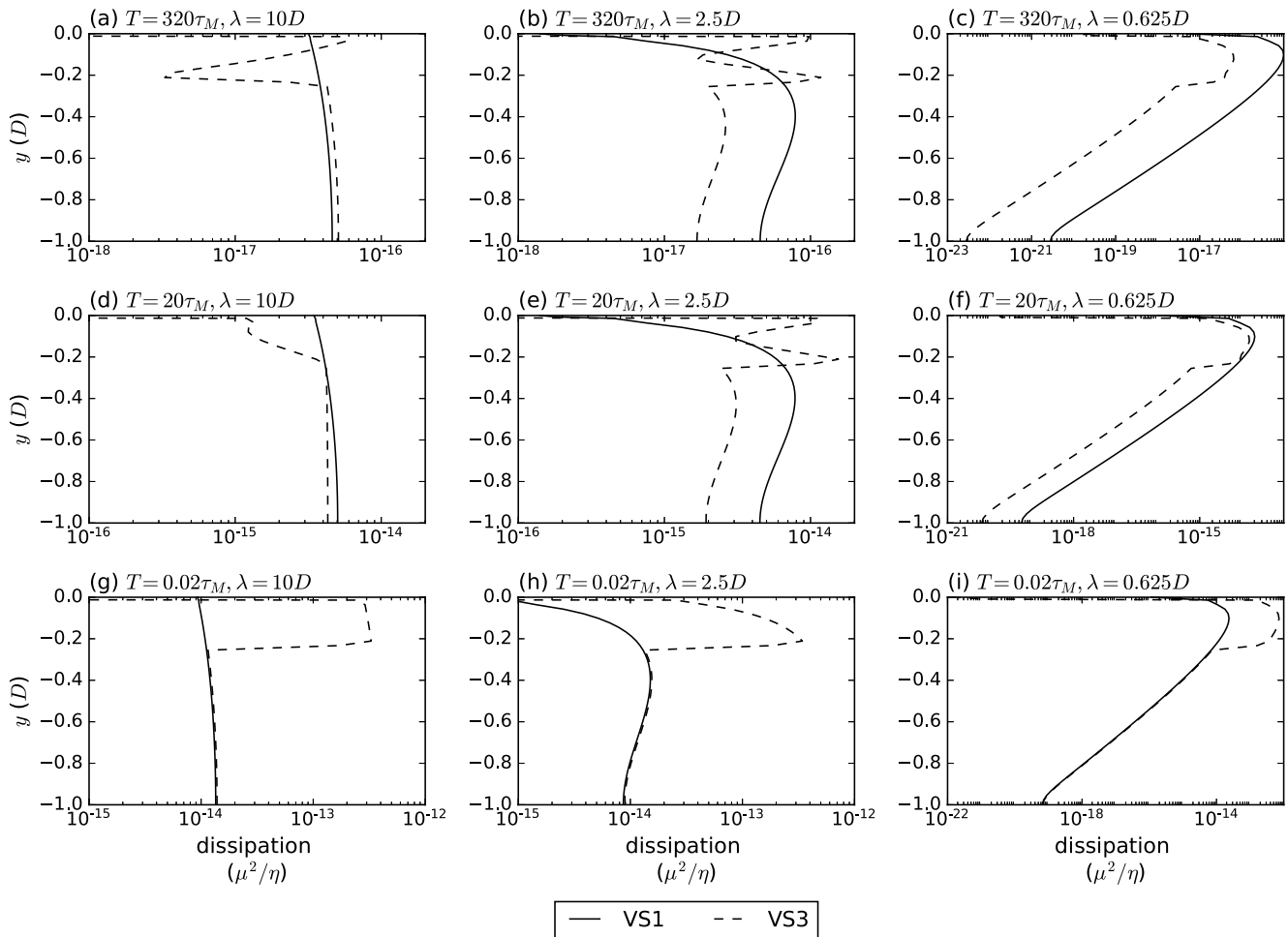


**Figure 8.** Plots of the averaged (over both time and space) dissipation rate versus depth for VS1 (solid line) and VS3 (dashed line) cases with periods (top row)  $320\tau_M$ , (middle row)  $20\tau_M$ , and (bottom row)  $0.02\tau_M$ , and with wavelengths (first column)  $10D$ , (middle column)  $2.5D$ , and (last column)  $0.625D$ .

surface is converted to heat by viscous dissipation. Figure 9a shows the energy flux for both dissipation (solid lines) and work (dashed lines) versus period for VS1 and VS3 at wavelength  $1.25D$  (note that the results for VS1 and VS2 are again nearly identical). As seen previously in Figure 4, for a given viscoelastic structure, the energy flux associated with the work increases with decreasing loading period or faster loading rate. This result is confirmed here by our models with a wide range of periods (Figure 9a). However, the energy flux for work does not increase uniformly with loading rate, and it is approximately constant at periods between  $1\tau_M$  and  $10\tau_M$  for VS1/VS2 models and at periods of  $\sim 0.1\tau_M$  for VS3 model (Figure 9a). For periods between  $0.01\tau_M$  and  $10\tau_M$ , the energy flux for work for VS3 is significantly larger than that for VS1/VS2, while for other periods, the energy flux for work for VS1/VS2 is larger.

The dissipation displays significantly different characteristics from the work done at the surface. For a given viscoelastic model (e.g., VS1), the energy flux for dissipation is constant for periods that are less than a threshold period (e.g.,  $\sim 10\tau_M$  for VS1), but the energy flux decreases with increasing period for longer periods (Figure 9a). At short periods, the energy flux for dissipation is very small compared to that for work at the surface (Figure 9a). However, at long periods, the dissipation is nearly equal to the work done at the surface. The system's efficiency in converting mechanical energy to heat is defined as the time-averaged energy flux for dissipation divided by that for work. For VS1/VS2 models, the efficiency is low at short periods and approaches a maximum of 1 at period of  $\sim 1\tau_M$  (Figure 9b). The energy flux for dissipation for VS3 is more than 1 order of magnitude larger than that for VS1/VS2 for short periods, but is smaller than that for VS1/VS2 for period larger than  $\sim 10\tau_M$  (Figure 9a, and also Figure 5). For VS3, the efficiency approaches a maximum of 1 at period of  $\sim 0.1\tau_M$ , compared with  $1\tau_M$  period

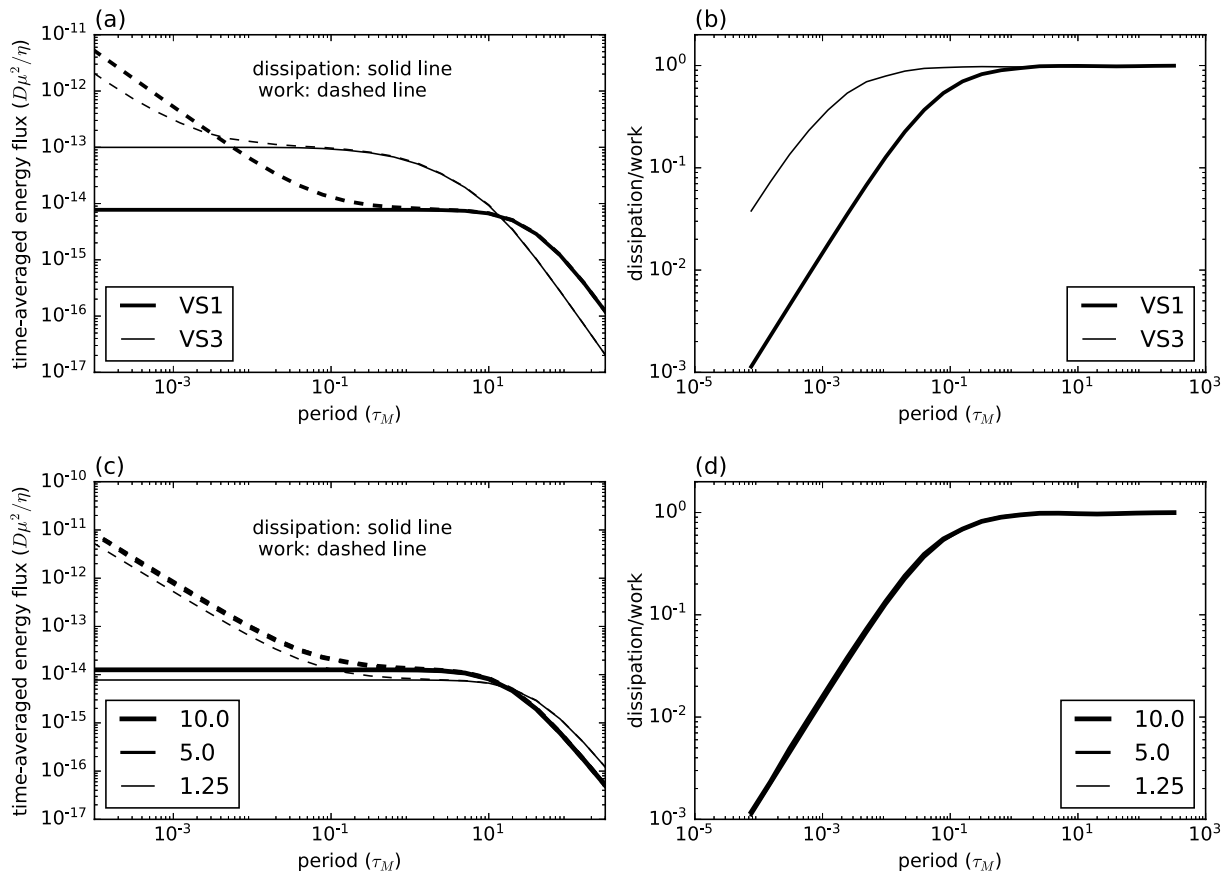


**Figure 9.** (a) Time-averaged energy flux for work done at the surface and dissipation over the loading cycle for each period for VS1 and VS3 viscosity structures at wavelength  $1.25D$ . The solid lines show dissipation, and the dotted lines show work. (b) Efficiency, calculated as dissipation divided by work versus period for each viscosity structure. Panels (c and d) are the same as in (a and b) for VS1 for wavelengths  $1.25D$ ,  $5.0D$  and  $10D$ .

for VS1/VS2 (Figure 9b). This is because VS3 has a lower effective mantle viscosity than VS1 and VS2 due to its weak upper mantle layer, and so the effective Maxwell time for VS3 will be smaller.

Figures 9c and 9d show the energy fluxes of the work and dissipation and efficiency versus period for three different wavelengths for VS1. The energy fluxes for work and dissipation and the efficiency of the system are in general not very sensitive to wavelength (Figures 9c and 9d).

## 4. Discussion

This study formulates 2-D viscoelastic (Maxwellian) models of surface loading to understand the general controls on the energetics of planetary mantles associated with exogenic forcing. Specifically, the model calculations examine the effects of period and wavelength of loading and mantle viscosity structure on the work done by surface forces and dissipative and elastic energies in the mantle during the loading process. Here is an overview of our main results and discussions of implications of the results for some loading systems.

### 4.1. Characteristics of Surface Forced Viscous Dissipation

This study demonstrates through both analysis and numerical modeling that the dissipative heat and elastic energy in the media are balanced by the work done by forces at the surface including the loading force and restoring force associated with the topography, regardless of mantle viscosity and loading period and wavelength (Equation 16, Figures 2e and 4). However, mantle viscosity and loading period have important influence on the work done by forces at the surface and partitioning of dissipative heat and elastic energy. In particular, the period of the loading force strongly affects how the work done at the surface is partitioned between dissipative and elastic terms

(Figures 4 and 9). For long periods (Figure 4a), nearly all the input work is converted to dissipative heat with very little elastic energy involved, while for short periods (Figure 4c), nearly all the input work is stored and released elastically with very little dissipation. Therefore, at the long and short period limits, the work done at the surface is generally in phase with either dissipative heat generation or elastic energy. However, at intermediate periods (Figure 4b), all three energy terms are similar in amplitude and are slightly out of phase from one another, as the conversion from mechanical to thermal energy introduces the time lag which is characteristic of dissipative systems.

For a given amplitude of the load (e.g., equivalent to 1 m thick mantle material), the energy flux (or the power) associated with the work done by surface forces generally increases with decreasing period (Figures 4, 9a and 9c). The energy flux for dissipative heat also generally increases with decreasing period but remains constant for period shorter than some characteristic period ( $\sim 10\tau_M$  for VS1 and  $\sim 1\tau_M$  for VS3) (Figures 9a and 9c). The dissipation rate does not depend strongly on loading wavelength (Figure 9c).

Viscosity structure (e.g., uniform viscosity VS1 vs. VS3 with a factor of 30 viscosity reduction in the upper mantle) has significant effects on both the work done at the surface and dissipation. For long periods ( $> \sim 10\tau_M$ ), the energy flux of dissipation for VS1 is larger than that for VS3 (Figures 8a and 9a), but for short periods ( $< \sim 10\tau_M$ ), VS3 models produce significantly more (i.e., by a factor of 10 for periods  $< \sim 1\tau_M$ ) dissipation than VS1 (Figures 5c and 9a). The same trend exists for the work done at the surface, but at very short periods VS1 models produce more work at the surface than VS3 models (Figure 9a). The periods at which these transitions occur and the increase in dissipative heat for VS3 likely depend on the viscosity reduction in the upper mantle, which may be an interesting topic for future studies.

An interesting feature for both VS1 and VS3 models is that at the short period (elastic) limit, energy flux of the work done at the surface increases nearly linearly with decreasing period  $T$ , while energy flux of dissipation is a constant (i.e.,  $P_{\text{work}} = C_1/T$ , and  $P_\phi = C_2$ , where  $C_1$  and  $C_2$  are constants) (Figure 9a). That is, over a period  $T$ , the work done by surface net force  $\Delta W$  (Equation 7) is a constant independent of  $T$ , or  $\Delta W = C_1$ , while dissipative heat  $\phi$  is linearly proportional to  $T$  or  $\phi = C_2T$ . For the long period (viscous) limit,  $P_{\text{work}}$  and  $P_\phi$  with the same amplitudes both decrease with increasing  $T$  but with a slope that is steeper than 1 (Figure 9a). The simplicity of the results at the two limits suggests that a simple model may be formulated for the limiting cases, which we leave for future studies.

For models with uniform viscosity (VS1), the spatial distribution of dissipation depends on loading wavelength but is independent of loading period (Figures 6 and 8). Loading at short wavelengths produces dissipation at shallow depths, while loading at long wavelengths generates dissipation that extends deeply. Particularly, for short wavelengths, dissipation concentrates at shallow depths but does not vary in the horizontal direction, whereas for long wavelengths, dissipation concentrates on the two edges of the model box. The loading function is a cosine function of the horizontal coordinate (i.e., Equation 3) such that at the center of the box there is very little pressure force and thus very little topography produced. At long wavelengths, the pattern of dissipation mirrors this, with dissipation maximums occurring directly underneath the areas with the greatest topography (the box edges) (Figures 6a, 6d and 6g). At short wavelengths, however, there is no such pattern in the dissipation (Figures 6c, 6f and 6i).

For models with the weak upper mantle (VS3), the spatial distribution of dissipation depends on both period and wavelength. At long periods and long wavelengths, dissipation is concentrated in the lower mantle (Figures 7a and 7d), but in all other cases dissipation is concentrated in the upper mantle (Figures 7 and 8). The dissipation occurs mostly at the edges of the box or near the viscosity interface for all the cases except for short wavelength and short period for which horizontal variation in dissipation is minimal (Figures 7i and 8i). That the dissipation concentrates in the weak upper mantle at intermediate and short wavelengths and long periods (i.e.,  $\sim 300\tau_M$ ) is consistent with Hanyk et al. (2005) and Huang et al. (2018).

#### 4.2. Applications to the Present-Day Earth

The Earth's mantle is estimated to cool at a rate of about 70 K/Ga, which suggests that the early Earth's mantle may have been up to 300 K hotter than the present-day (G. F. Davies, 1999). This implies that early Earth may have had a viscosity of only  $10^{19}$  Pa-s, or even smaller at shallower depths, due to pressure-dependence of viscosity (Karato, 2008). To examine how surface loading-induced dissipation processes may have evolved throughout



Earth's history, the results for VS3 which most closely models the Earth's interior are rescaled for several reference viscosities (i.e., the lower mantle viscosity), ranging from  $10^{22}$  Pa·s, which is representative of Earth at present-day (e.g., Mao & Zhong, 2021; Mitrovica & Forte, 2004), to  $10^{18}$  Pa·s, which may be representative of the early Earth.

Figures 10a and 10b show the time-averaged energy flux of dissipation and work for different periods of VS3 with loading wavelengths  $1.25D$  (i.e., Figures 9a) and  $5D$ , respectively, scaled for mantle thickness  $D = 2,900$  km, shear modulus  $\mu = 7 \times 10^{10}$  Pa and five different reference viscosities ( $10^{18}$ – $10^{22}$  Pa·s) under the application of a 1 m rock load. As expected from time scale  $\tau_M = \eta/\mu$  and energy flux scale  $D\mu^2/\eta$ , the curves with different reference viscosities are identical in shape but shifted in both horizontal and vertical axes that now have units. For short periods, the smaller the reference viscosity  $\eta$ , the larger the energy flux of dissipation (Figure 10). However, for long periods, the opposite is true. The energy flux of work done at the surface increases with decreasing period but does not depend on reference viscosity at very short periods. That is, if the curves for the work done for different viscosities in Figure 10 are extended toward very short period, they all plot along the same line. These results are simply a consequence of re-scaling for the energy flux of dissipation that is independent of period  $T$  (or  $\sim T^0$ ) at short periods but depends on  $1/T^p$  with  $p > 1$  at long periods, while the energy flux of work at short periods depends on  $1/T$  (Figure 10a).

The volumetric dissipation is estimated for several processes on present day Earth to compare with the amount of heat produced by radiogenic decay and the total heat flux. During the Early Pleistocene, glaciation-deglaciation cycles had a period of about 40,000 years and since the Mid-Pleistocene Transition they have had a period of about 100,000 years (e.g., Berends et al., 2021). Considering an amplitude of ice sheet thickness variation of 2,500 m (i.e.,  $\sim 750$  m of rock height) at the peak of glaciation and a wavelength of 3,600 km (i.e., about  $1.25D$  which is more representative of the Fennoscandian ice sheet), and a reference viscosity of  $10^{22}$  Pa·s, Figure 10a indicates that the energy flux of dissipation is  $\sim 5 \times 10^{-9}$  W/m<sup>2</sup> for loading period 100,000 years with 1 m rock load. This leads to  $\sim 3 \times 10^{-3}$  W/m<sup>2</sup> (i.e., 3 mW/m<sup>2</sup>) for 2,500 m ice load amplitude, given that the energy scales with square of the load amplitude. Assuming the dissipation occurring uniformly in the mantle leads to a volumetric dissipation rate of  $\sim 10^{-9}$  W/m<sup>3</sup> (i.e., dividing energy flux of 3 mW/m<sup>2</sup> by mantle thickness  $D$  of 2,900 km). The North American ice sheet may have a dominant wavelength of  $\sim 7,000$  km, and because the energy flux of dissipation is slightly smaller for longer wavelengths for long periods (Figures 9c and 10), the estimated surface heat flux and volumetric dissipation rate are  $\sim 2$  mW/m<sup>2</sup> and  $7 \times 10^{-10}$  W/m<sup>3</sup>, respectively. These estimates are 2%–4% of the averaged present-day surface heat flux of 87 mW/m<sup>2</sup> (e.g., Jaupart et al., 2007) and 5%–7% of radiogenic heat generation of  $1.4 \times 10^{-8}$  W/m<sup>3</sup> for the bulk silicate Earth (Sramek et al., 2013; Workman & Hart, 2005). Han

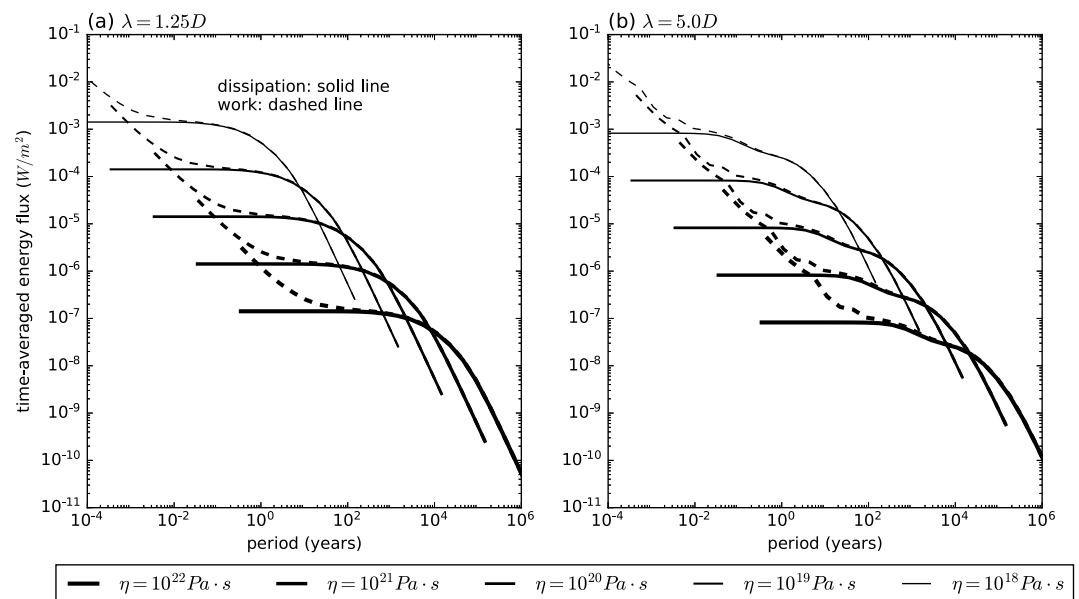


**Figure 10.** Time-averaged energy flux plotted versus period for several reference viscosity values for VS3 under a 1 m rock load at wavelengths (a)  $1.25D$  and (b)  $5D$ .

et al. (2005) and Huang et al. (2018) considered realistic ice loading models and found that the time-averaged surface heat flux from the loading-induced dissipation for the last glaciation-deglaciation cycle is  $\sim 0.03$  TW. Considering that North American and Fennoscandian ice sheets may only cover  $\sim 2\%$  of the Earth's surface, their surface heat flux results are broadly consistent with ours.

If a glacial cycle period 40,000 years for the Early Pleistocene is used, the estimated surface heat flux and dissipation rate for wavelength 3,600 km will be increased by a factor of 3 (Figures 10a) to  $9 \text{ mW/m}^2$  and  $3 \times 10^{-9} \text{ W/m}^3$ , respectively, suggesting the important influence of loading period on the dissipation. Such dissipative heating, if lasting for a significant amount of time, may have significant effects on mantle dynamics, especially considering that the heating is likely concentrated in the upper mantle (e.g., Hanyk et al., 2005). As another example, the results are also scaled for seasonal change in the Amazon River basin, again with wavelength of 3,600 km, a period of 1 year, and a 0.3 m water load (or 0.1 m rock load). The energy flux of dissipation is estimated at  $\sim 1.5 \times 10^{-7} \text{ W/m}^2$  (Figure 10a), which is insignificant compared with the surface heat flux.

### 4.3. Implications for the Early Earth and Other Planetary Bodies

Here we discuss possible dissipation rate for the early Earth conditions, focusing on loading processes of different periods with reduced mantle viscosities. Long-term climate processes such as glacial cycles are mostly driven by insolation variations that are controlled by the Earth's orbital parameters including eccentricity, obliquity, and precession rate (Berends et al., 2021; Milankovic, 1941). However, given that the energy flux of dissipation decreases with decreasing viscosity at relatively long periods (Figure 10), it is unlikely that these long-term climate driven processes would contribute any significant dissipative heating in the mantle. However, it is possible that climate related processes at relatively short periods (e.g., annual or decadal changes), if they are associated with significant surface mass movement, may produce potentially significant dissipation rate for the early Earth's mantle, because at short periods the dissipation increases with decreasing viscosity (Figure 10).

Tidal forcing at periods of around 1 day may cause significant dissipative heating in the early Earth's mantle, particularly because of relatively short distance between the Earth and the Moon at that time. The most important tidal potential on the Earth is at harmonic degree 2 raised by the Moon, and for simplicity assuming a circular lunar orbit with zero obliquity (but obliquity tides can be important for other systems, e.g., Tyler, 2009), the spatial component of the degree-2 and order-0 tidal potential at the Earth's surface can be written as (e.g., Agnew, 2007):

$$V = \frac{GM_m R^2}{a^3} P_{20}(\cos \theta), \quad (18)$$

where  $G$  is the gravitational constant,  $M_m$  is the mass of the Moon,  $R$  is the Earth's mean radius,  $a$  is the radius of the lunar orbit, and  $\theta$  is the co-latitude. To model tidal deformation for incompressible mantle, the tidal force needs to be applied to the surface and the core-mantle boundary (Qin et al., 2018). Our loading model here only considers forcing at the surface in 2-D Cartesian box, but the model may still provide some useful insight. Equating the tidal potential in Equation 18 to the gravitational potential produced by a degree-2 and order-0 mass anomaly of surface density amplitude  $\rho\delta$ :

$$\frac{4\pi GR\rho\delta}{5} P_{20}(\cos \theta) = \frac{GM_m R^2}{a^3} P_{20}(\cos \theta), \quad (19)$$

leads to an estimated height of equivalent rock load  $\delta \sim 1$  m, where  $a = 60R$  is the present-day distance between the Moon and Earth,  $M_m = 7.35 \times 10^{22} \text{ kg}$ ,  $R = 6,370 \text{ km}$ , and  $\rho = 3,300 \text{ kg/m}^3$ . Because our model does not consider the loading at the core-mantle boundary, it is reasonable to double  $\delta$  to 2 m. From Figure 10b for a reference viscosity of  $10^{22} \text{ Pas}$  and loading wavelength of  $5D$ , which resembles degree-2 wavelength, the energy flux of dissipation is  $\sim 8 \times 10^{-8} \text{ W/m}^2$  for 1 m rock load or  $3.2 \times 10^{-7} \text{ W/m}^2$  for 2 m rock load. The latter corresponds to a total power of  $1.3 \times 10^8 \text{ W}$ , which is insignificant compared with the present-day heat flux value.

It has been proposed that  $a$  is  $\sim 32R$  at 4 Ga, and is even smaller before 4 Ga, based on calculations of lunar fossil bulge formation and orbital evolution (Qin et al., 2018). This implies that tidal forcing at 4 Ga was  $\sim 10$  times larger than it is today. Together with enhanced dissipation for a reduced reference mantle viscosity of  $10^{19} \text{ Pas}$  (Figure 10b), the total power of tidal dissipation for the early Earth's mantle may be  $\sim 13$  TW from degree 2 and order 0 loading or  $\sim 26$  TW for all degree 2 loading terms. This tidal heating may have important dynamic

implications for mantle melting in and thermal evolution of the early Earth, considering that the dissipation may occur entirely in the weak upper mantle or weak layer even at degree-2 long wavelengths (Figures 7 and 8g).

That tidal dissipation may concentrate at shallow depths with small viscosity has special implications for other planetary bodies for which tidal heating is important, for example, Io or the Moon. The pressure dependencies of mantle rheology, solidus and adiabat tend to give rise to a reduced mantle viscosity at shallow depths. The enhanced tidal dissipation at the relatively weak shallow depth may lead to increased temperature there, which reduces the viscosity even more, as pointed out by Steinke et al. (2020). This positive feedback process may be responsible for a weak asthenosphere and even global-scale melting such as that on Io, and it also suggests that the deep mantle of Io may not be affected significantly by the tidal heating. As discussed earlier, a large number of studies have explored various tidal heating effects on Io and other icy satellites (e.g., Beuthe, 2013; Bierson & Nimmo, 2016; A. G. Davies et al., 2015; Hamilton et al., 2013; Ross & Schubert, 1985; Sotin et al., 2002; Tobie et al., 2005, 2008).

## 5. Conclusions

This study examined the dissipative behavior of a viscoelastic solid under a surface load to understand the potential contribution of dissipative heat caused by exogenic forces to the energy budget of the Earth and other solid celestial bodies. Using a linear Maxwell rheology and assuming an incompressible and non-accelerating material, we computed solutions to the viscoelastic loading problem for 345 different cases with varying viscosity structure, loading wavelength, and loading period. The results were then analyzed to understand the controls on the partitioning of dissipative and elastic energy terms and their spatial distributions, and to estimate how much dissipative heating occurs for present-day and early Earth as a result of exogenic forces.

We demonstrated through analysis of the energy balance that the dissipative heat and elastic energy always balance the work done at the surface by loading force and restoring force associated with the topography, which is verified by our numerical modeling. Our results show that the partition of energy between dissipative and elastic terms is strongly dependent on the loading period, and that at long periods (i.e., viscous limit), the work done at the surface is consumed by dissipative heat with negligible elastic energy involved, while at short periods (elastic limit), the work done at the surface is accommodated mostly by elastic energy. The average dissipation flux in the elastic limit is constant and independent of periods, while the energy flux of the work done at the surface decreases linearly with increasing period, suggesting that dissipation in the elastic limit has an upper bound, independent of the work done at the surface. In the viscous limit, the average dissipation flux and the work are nearly equal and decrease with a slope greater than 1 as period increases.

Dissipation rate is smaller for longer loading wavelength. Viscosity structure controls both the magnitude and distribution of dissipation rate. Models with a weak upper mantle generate significantly more dissipation rate at relatively short periods than those with uniform mantle viscosity. However, for relatively long periods, the opposite is true. The spatial distribution of dissipation depends on wavelength but not on period for a uniform viscosity structure, and on both period and wavelength for a layered viscosity structure. For models with a weak upper mantle layer, dissipation is concentrated in the upper mantle in nearly all cases except those with very long wavelengths and long periods, suggesting that most heat generation will be concentrated at shallow depths on bodies with such viscosity structures.

We find that our models produce estimates for glaciation- and deglaciation-forced dissipation that are broadly consistent with those found in other studies. For a shorter glacial period (e.g., ~40,000 years), such as that of the Early Pleistocene, dissipative heating may lead to 3–9 mW/m<sup>2</sup> surface heat flux in glaciated regions, and if such glacial cycles last for sufficiently long time, the resulting dissipative heat may have a significant effect on mantle dynamics, especially since dissipation is likely concentrated in the upper mantle. On present-day Earth, we find that tidal heating produces an insignificant amount of heat, but for early Earth with a smaller mantle viscosity and larger forcing amplitude, it may have produce ~30 TW global surface heat flux, representing a significant fraction of the global heat flux and influencing mantle melting and cooling during that time. The finding that tidal dissipation is concentrated at shallow depths even at very long wavelengths has important implications for the dynamic evolution of the early Earth and any planetary body where tidal heating is important, such as Io. Heating concentrated in a weak layer will increase its temperature and thus decrease its viscosity, making the layer weaker, and creating a positive feedback system in the upper mantle. This may contribute to the formation of

a weak asthenosphere and global scale melting at shallow depths, and also suggests that the deep mantle of such systems (e.g., Io) may not be significantly affected by tidal heating.

This study is limited by the simplicity of our model, first in that we used a 2D Cartesian geometry rather than a full spherical treatment of the problem, and second in our assumptions of uniform shear modulus and viscosity and Maxwell rheology. The Maxwell rheology may not be a good representation of the deformational behavior of mantle materials at short periods, and variable shear modulus and viscosity may affect the loading response (e.g., Steinke, 2021). The Cartesian model may present different spatial patterns of dissipation than a spherical model due to the flat geometry, and because of the small size of the domain compared to the load. Future research into this topic using full spherical geometries would provide better understanding of behaviors under tidal forcing, as these are not necessarily well approximated by a surface loading force, and the use of more sophisticated rheology models (e.g., Huang et al., 2018) is likely necessary to understand more about how these bodies react to all types of exogenic forces. Even with these shortcomings, we believe that this study represents an important step in understanding the dynamics of dissipative heating in planetary bodies.

### Data Availability Statement

The CitcomVE package and the input files used in this study can be found at <https://zenodo.org/record/6677595>. Additional model input parameters are given in Tables 1–3.

### Acknowledgments

This work is supported by NASA ESI 80NSSC18K0470 and NSF EAR-1940026. The authors would like to thank Dr. Wouter van der Wal and an anonymous reviewer for their helpful reviews. The code and the model results produced in this study are available upon request.

### References

- Agnew, D. C. (2007). Earth tides. *Treatise on Geophysics*, 3, 163–195. <https://doi.org/10.1016/b978-044452748-6.00056-0>
- Berends, C. J., Köhler, P., Lourens, L. J., & van de Wal, R. S. W. (2021). On the cause of the mid-Pleistocene transition. *Reviews of Geophysics*, 59(2), e2020RG000727. <https://doi.org/10.1029/2020RG000727>
- Beuthe, M. (2013). Enceladus's crust as a non-uniform thin shell: I tidal deformations. *Icarus*, 302, 145–174. <https://doi.org/10.1016/j.icarus.2017.11.009>
- Bierson, C. J., & Nimmo, F. (2016). A test for Io's magma ocean: Modeling tidal dissipation with a partially molten mantle. *Journal of Geophysical Research*, 121(11), 2211–2224. <https://doi.org/10.1002/2016je005005>
- Davies, A. G., Veeder, G. J., Matson, D. L., & Johnson, T. V. (2015). Map of Io's volcanic heat flow. *Icarus*, 262, 67–78. <https://doi.org/10.1016/j.icarus.2015.08.003>
- Davies, G. F. (1999). *Dynamic Earth: Plates, plumes and mantle convection*. Cambridge University Press.
- Hager, B. H., & Richards, M. A. (1989). Long-wavelength variations in Earth's geoid: Physical models and dynamical implications. *Philosophical Transactions of the Royal Society of London - A*, 328, 309–327.
- Hamilton, C. W., Beggan, C. D., Still, S., Beuthe, M., Lopes, R. M., Williams, D. A., et al. (2013). Spatial distribution of volcanoes on Io: Implications for tidal heating and magma ascent. *Earth and Planetary Science Letters*, 361, 272–286. <https://doi.org/10.1016/j.epsl.2012.10.032>
- Hanyk, V., Matyska, C., & Yuen, D. A. (2005). Short time-scale heating of the Earth's mantle by ice-sheet dynamics. *Earth Planets and Space*, 57(9), 895–902. <https://doi.org/10.1186/bf03351867>
- Huang, P. P., Wu, P., & van der Wal, W. (2018). Effects of mantle rheologies on viscous heating induced by Glacial Isostatic Adjustment. *Geophysical Journal International*, 213(1), 157–168. <https://doi.org/10.1093/gji/ggx535>
- Jaupart, C., Labrosse, S., & Mareschal, J. C. (2007). Temperatures, heat and energy in the mantle of the Earth. In *Treatise on Geophysics* (Vol. 7, pp. 253–303). Elsevier B. V.
- Karato, S. I. (2008). *Deformation of Earth materials: An introduction to the rheology of Solid Earth*. Cambridge University Press.
- Mao, W., & Zhong, S. (2021). Constraints on mantle viscosity from intermediate wavelength geoid anomalies in mantle convection models with plate motion history. *Journal of Geophysical Research*, 126(4), e2020JB021561. <https://doi.org/10.1029/2020JB021561>
- Milankovic, M. (1941). Kanon der Erdbestrahlung und seine Anwendung auf das Eiszeitenproblem.
- Mitrovica, J. X., & Forte, A. M. (2004). A new inference of mantle viscosity upon joint inversion of convection and glacial isostatic adjustment data. *Earth and Planetary Science Letters*, 225(1), 177–189. <https://doi.org/10.1016/j.epsl.2004.06.005>
- Moresi, L., & Solomatov, V. S. (1995). Numerical investigation of 2-D convection with extremely large viscosity variations. *Physics of Fluids*, 7(9), 2154–2162. <https://doi.org/10.1063/1.868465>
- Ojakangas, G. W., & Stevenson, D. J. (1989). Thermal state of an ice shell on Europa. *Icarus*, 81(2), 220–241. [https://doi.org/10.1016/0019-1035\(89\)90052-3](https://doi.org/10.1016/0019-1035(89)90052-3)
- Qin, C., Zhong, S., & Philips, R. (2018). Formation of the lunar fossil bulges and its implication of the early Earth and Moon. *Geophysical Research Letters*, 45, 1286–1296. <https://doi.org/10.1002/2017GL076278>
- Qin, C., Zhong, S., & Wahr, J. (2014). A perturbation method and its application: Elastic tidal response of a laterally heterogeneous planet. *Geophysical Journal International*, 199(2), 631–647. <https://doi.org/10.1093/gji/ggu279>
- Roberts, J. H., & Nimmo, F. (2008). Tidal heating and the long-term stability of a subsurface ocean on Enceladus. *Icarus*, 194(2), 675–689. <https://doi.org/10.1016/j.icarus.2007.11.010>
- Ross, M. N., & Schubert, G. (1985). Tidally forced viscous heating in a partially molten Io. *Icarus*, 64(3), 391–400. [https://doi.org/10.1016/0019-1035\(85\)90063-6](https://doi.org/10.1016/0019-1035(85)90063-6)
- Ross, M. N., & Schubert, G. (1986). Tidal dissipation in a viscoelastic planet. *Journal of Geophysical Research*, 91(B4), D447–D452. <https://doi.org/10.1029/jb091ib04p0447>
- Ross, M. N., & Schubert, G. (1987). Tidal heating in an internal heating model of Europa. *Nature*, 325(6100), 133–144. <https://doi.org/10.1038/325133a0>

- Segatz, M., Spohn, T., Ross, M. N., & Schubert, G. (1988). Tidal dissipation, surface heat flow, and figure of viscoelastic models of Io. *Icarus*, 75(2), 187–206. [https://doi.org/10.1016/0019-1035\(88\)90001-2](https://doi.org/10.1016/0019-1035(88)90001-2)
- Sotin, C., Head, J. W., & Tobie, G. (2002). Europa: Tidal heating of upwelling thermal plumes and the origin of lenticulae and chaos melting. *Geophysical Research Letters*, 29(8), 1233–74-4. <https://doi.org/10.1029/2001GL013844>
- Sramek, O., McDonough, W. F., Kite, E. S., Lekic, V., Dye, S. T., & Zhong, S. J. (2013). Geophysical and geochemical constraints on geoneutrino fluxes from Earth's mantle. *Earth and Planetary Science Letters*, 361, 356–366. <https://doi.org/10.1016/j.epsl.2012.11.001>
- Steinke, T. (2021). *The curious case of Io—Connections between interior structure, tidal heating and volcanism* (Ph.D. Thesis). Delft University of Technology. <https://doi.org/10.4233/uuid:9e875752-05bc-4dd8-9bdd-77e18cf3c43f>
- Steinke, T., Hu, H., Höning, D., Van der Wal, W., & Vermeersen, B. (2020). Tidally induced lateral variations of Io's interior. *Icarus*, 335, 113299. <https://doi.org/10.1016/j.icarus.2019.05.001>
- Tobie, G., Cadek, O., & Sotin, C. (2008). Solid tidal friction above a liquid water reservoir as the origin of the south pole hotspot on Enceladus. *Icarus*, 196(2), 642–652. <https://doi.org/10.1016/j.icarus.2008.03.008>
- Tobie, G., Mocquet, A., & Sotin, C. (2005). Tidal dissipation within large icy satellites: Applications to Europa and Titan. *Icarus*, 177(2), 534–549. <https://doi.org/10.1016/j.icarus.2005.04.006>
- Turcotte, D. L., & Schubert, G. (2002). *Geodynamics*. Cambridge University Press.
- Tyler, R. (2011). Tidal dynamical considerations constrain the state of an ocean on Enceladus. *Icarus*, 211(1), 770–779. <https://doi.org/10.1016/j.icarus.2010.10.007>
- Tyler, R. H. (2009). Ocean tides heat Enceladus. *Geophysical Research Letters*, 36(15), L15205. <https://doi.org/10.1029/2009gl038300>
- Tyler, R. H., Henning, W. G., & Hamilton, C. W. (2015). Tidal heating in a magma ocean within Jupiter's moon Io. *The Astrophysical Journal - Supplement Series*, 218(2), 22. <https://doi.org/10.1088/0067-0049/218/2/22>
- Workman, R. K., & Hart, S. R. (2005). Major and trace element composition of the depleted MORM mantle (DMM). *Earth and Planetary Science Letters*, 231(1–2), 53–72. <https://doi.org/10.1016/j.epsl.2004.12.005>
- Wu, P., & Peltier, W. R. (1982). Viscous gravitational relaxation. *Geophysical Journal of the Royal Astronomical Society*, 70(2), 435–485. <https://doi.org/10.1111/j.1365-246x.1982.tb04976.x>
- Zhong, S. (1997). Dynamics of crustal compensation and its influences on crustal isostasy. *Journal of Geophysical Research*, 102(B7), 15287–15299. <https://doi.org/10.1029/97jb00956>
- Zhong, S., Paulson, A., & Wahr, J. (2003). Three-dimensional finite-element modelling of Earth's viscoelastic deformation: Effects of lateral variations in lithospheric thickness. *Geophysical Journal International*, 155(2), 679–695. <https://doi.org/10.1046/j.1365-246x.2003.02084.x>
- Zhong, S., & Watts, A. B. (2013). Lithospheric deformation induced by loading of the Hawaiian Islands and its implications for mantle rheology. *Journal of Geophysical Research: Solid Earth*, 118(11), 6025–6048. <https://doi.org/10.1002/2013jb010408>